IJES *Iranian Journal of Earth Sciences*
Vol. 12, No. 4, 2020, 266-279.

Application of landsat imageries for mapping post-earthquake landslide, case study: 2012 Ahar-Varzegan earthquake, NW Iran

Leila Khodaei Geshlag*[1], Shahram Roostaei[1], Davood Mokhtari[1], Kalil Valizadeh[1]

1. Department of Geomorphology, University of Tabriz, Iran

Received 6 May 2019; accepted 30 January 2020

Abstract

The 2012 Ahar-Varzegan earthquake and its aftershocks have not only caused huge damage with a severe loss of life and property but also induced many geo-hazards with the major type of collapse, creep, slip, debris flow, and fallings that are generally considered as landslide in this study which can cause continuous threats to the affected region. in this study, a semi-automated geo-hazard detection method has been presented to determine the Landslides due to 2012 Ahar-Varzaghan earthquake in area from Ahar to Varzaghan by the use of bi- temporal Landsat images from before and after the earthquake. The accuracy of the results was checked out using field observations, Google Earth images and the error matrix. The results of the visual validation with the Google Earth images showed that the used method can detect landslids with relatively high accuracy.The images of landsat5 and 8 Because of their multispectral advantages can be used as a suitable data source for research on Instabilities. Finally, the validating results obtained by using the error matrix showed the total accuracy of 92.1% and kappa coefficient was 0.99. So based on the results obtained from the above method, the landslides were distributed mainly in slopes between 15 and 40 degrees and the height distribution of instabilities of 1420 to 2000 meters. Also based on vegetation indices, density of landslides have been increased after the earthquake. Generally unstabel slopes are located along river valleys and roads in mountain regions with deep valleys and steep slopes. According to the nature of present study, the obtained result can be useful for environmental planners and project developers.

Keywords: *Landsat-5 and 8, Landslide, Ahar-Varzegan, Earthquake, Google Earth.*

1. Introduction

Earthquakes have long been recognized as a major cause of landslides. Earthquake-induced landslides have been documented from at least as early as 373 or 372 B.C. (Seed 1968). In addition to the loss of human life and the damage to property, the earthquake triggered numerous geo-hazards, majorly as the type of landslide. For example, the earthquake triggered a landslide on mount Everest that killed 21 persons, and another huge ice and rock landslide in the Langtang valley that caused hundreds of people to die or go missing and buried the entire village of Langtang (Lacroix 2016). Meanwhile, post-earthquake geo-hazards also caused substantial influences on mountain ecosystems, especially for the vegetation cover on slopes in the affected region, which in turn leads to high risk from secondary geo-hazards. According to the field and remote sensing-based investigations after the 2008 Wenchuan earthquake, which happened in Sichuan province, China, avalanches, landslides, and mixtures of landslides and constituted the main types of post-earthquake geo-hazards and persisted for several years after the earthquake (Huang et al. 2012, Wei et al. 2014, Zhao et. 2017). In spite of their geomorphic and economic significance, earthquake-induced landslides are not well understood (Keefer 1984) northwestern Iran is historically associated with destructive earthquakes mainly related to the north Tabriz fault (NTF).

The NTF stands at more than 50 km to the southeast of Ahar and Varzeghan cities, and expands along 150+ km in Nw-SE direction. During the past two decades, the Iranian seismic network has surveyed this area, and no important seismic activity has occurred in the northern region of the NTF (Yazdi et al. 2017). GPS-derived velocities at the NTF indicate a mainly north-northeast tectonic movement close to Ahar city, the recent average slip has been measured to be about 11 mm/year (Djamour et al. 2011).The recent relative quietness of this area was broken on 11 august 2012, with the occurrence of the earthquake sequence. Preliminary estimates placed, and the deaths were more than 330 persons and the number of injured persons was about 26,000 and overall, more than 50000 persons who have been resettled. Therefore, regarding the recent occurrence of this large earthquake in Ahar-Varzegan, it is very important to monitor these earthquake-induced geo-hazards, determine their spatial distribution, and support the process of geo-hazard risk assessment and mitigation. To obtain accurate information on earthquake-triggered geo-hazards, typically for landslides, two major methods be used, as previously described by Xu (2015). These methods are field investigation and remote sensing image interpretation. Although the field investigation is able to generate highly accurate and reliable results, it is cost-inefficient and labor-intensive, and it usually blocked in unreachable mountainous areas comparatively. Remote sensing technologies allow coverage of large regions at high frequency. This advantage enables remote sensing-based methods to become popular for monitoring

---
*Corresponding author.
E-mail address (es): khodaeileila@yahoo.com

landslides at different spatial-temporal scales (Travelletti et al. 2012, Martha et al. 2015, Zhao et al. 2017). Artificial visual interpretation is the typical method for landslide inventory. It avoids problems with missing a large number of landslides on small scales and can obtain detailed and comprehensive earthquake-triggered landslide inventories (Petschko et al. 2015, Xu 2015, Zhao et al. 2017). In addition to visual interpretation, the automatic extraction method has become popular in landslide detection due to its high efficiency and adjustable thresholds for landslide identification mean (Moosavi et al. 2014, Martha et al. 2015). Pixel-based and object-oriented automatic extraction approaches are two major types (Rastner et al. 2014). Pixel-based approaches mainly include the direct way by comparing the radiation intensity in each waveband and the post-classification way conducted by comparing pre-earthquake and post-earthquake classification maps (Nichol et al. 2005, Callaghan et al. 2015). The object-oriented automatic extraction method applied by generating a target polygon of pixels with the same characteristics based shape, color, texture, and context, and then extracting and classifying the characteristics of each target (Shi et al. 2015, Dou et al. 2015). In addition to the development in remote sensing-based methods, the availabilities of very high-resolution optical remote sensing images (Lacroix et al. 2013, Li et al. 2016, Zhao et al. 2017), point cloud, light detection, ranging data (Jaboyedoff et al. 2012, Zhan and Lai 2015),and Synthetic Aperture Radar (SAR) images and interferometric SAR technology (Milillo et al. 2014, Ciampalini et al. 2015, Zhao et al. 2017), promote the accurate mapping of earth surface because of their different advantages as ability to measure millimetre-scale changes in deformation over spans of days to years. So, it has applications for geophysical monitoring of natural hazards, for example earthquakes, volcanoes and landslides.

Other researchers had already studied changes in the earth surface. For example Moosavi and Ranjbar (2014) in order to monitor the landuse changes in Abarkooh mountain basin using techniques such as monitoring classification and accuracy evaluation after classification and application of base component analysis functions, Tasseled cap and image difference were used to monitor changes. (Emamgholi et al. 2007) investigated landuse changes using supervised classification method and modis images. (Moghimi et al. 2005) reviewed the methods to identify changes from bi-temporal satellite imagery using the base pixel and the base object approach. therefore, due to the previous researches in order to investigate the changes in the use of optical landsat images, in this paper, due to the lack of access to radar images such as Sentinel-1 or Envisat, for the time period of the Ahar-Varzaghan earthquake accurance, the changes investigate method has been used to study the changes using the pixel-based extraction method and landsat images - 8 and 5. Therefore, the main objective of this paper is to extract the slope instabilities arising from the 2012 Ahar-Varzaghan earthquake, such as collapse, creep, slip, debris flow, and fallings that are generally considered as landslide in this study.

2. Methodology

2. 1. Study Area

The studied region is a part of Ahar chai basin with an area of 1,593 square kilometers, which is one of the largest catchments in the East Azerbaijan province. The study area places in latitudes of 46° 35´ to 47° 10´ and longitudes of 38° 20´ to 38° 45´ (Roostaei 2000). Therefore, mentioned region is limited to the Arasbaran forests to the north, the eastern slopes of the Owrtat Sakhvor Mountain to the east, the eastern slopes of the Kohneloo Mountain to the west and the Aji chai basin to the south. The main river of this region is Ahar Chai, which eventually joins the river Ghara Soo and finally reaches to the Aras border river. The best ways to access this region is the Tabriz-Khajeh-Ahar-Caliber road, which passes through the area from north to south. Figure 1 shows the location of the study region from Varzaghan to Ahar. In terms of topography, the region includes the northern mountainous area, southern mountain range, mountain slopes range and Ahar plain.

2. 2. Remote Sensing Data

In this paper, landsat 5 images to date, 2014/09/15 and landsat 8 images to date, 2013/08/11 for row and passage number of 166-33 were used. As well as ARCGIS 10.4.1 and ENVI5 3 and SAGA 6.4 software were used to do the research.

2.3. Methodology

Based on the pixel-based extraction method, a semi-automated geo-hazard detection method was proposed to derive reliable earthquake-induced geo-hazard mapping results. Figure 2 shows the flowchart of the method. After radiometric normalizing of landsat images, a novel change detection method (Zhao et al, 2017) is applied to obtain difference images and map the earthquake-induced landslides. The last step involves validation of the landslide mapping results.

2.3.1. Image Preprocessing

Because all images were acquired from the USGS Earth Resources Observation and Science Center, terrain correction, as well as radiometric correction, atmospheric correction, and geometric precision correction, has been performed for Landsat- 8 &5 products (Vermote et al. 2016, Zhao et al. 2017).

2.3.2. Radiometric Normalization

Radiometric normalization is a particularly important step in this process. It is well known that changes between multitemporal remote sensing data can be caused by many other factors, including spatial, spectral, thematic

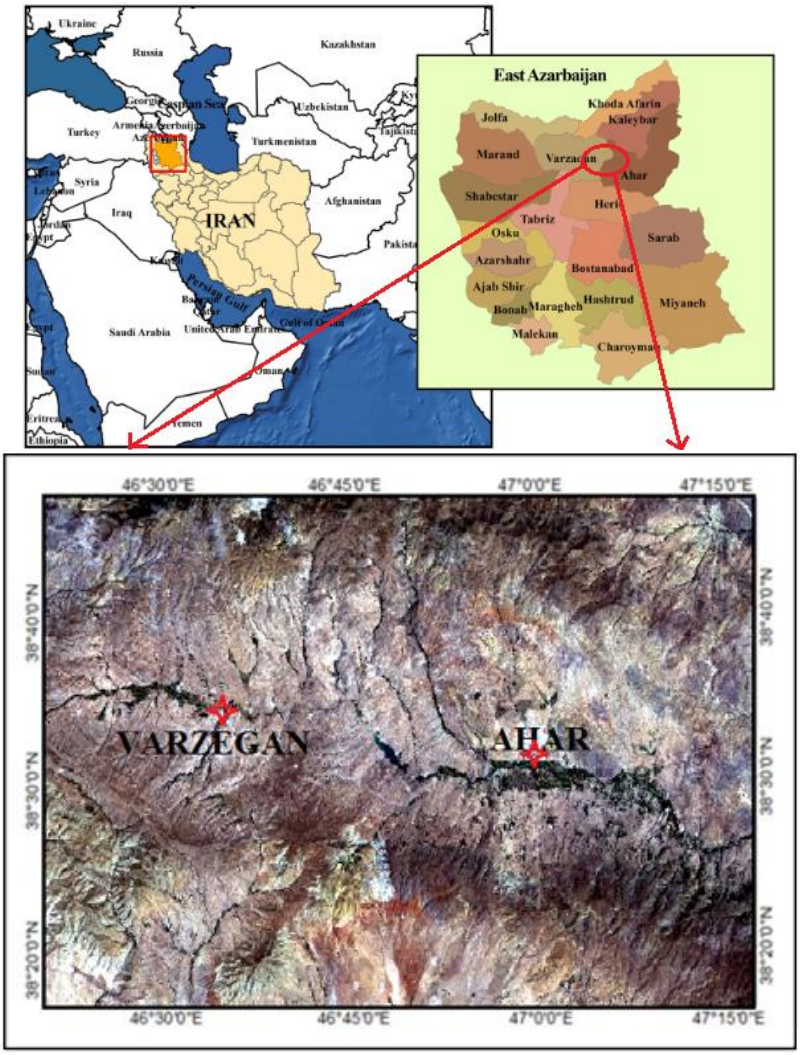

Fig1. Location of the study region from Varzaghan to Ahar.

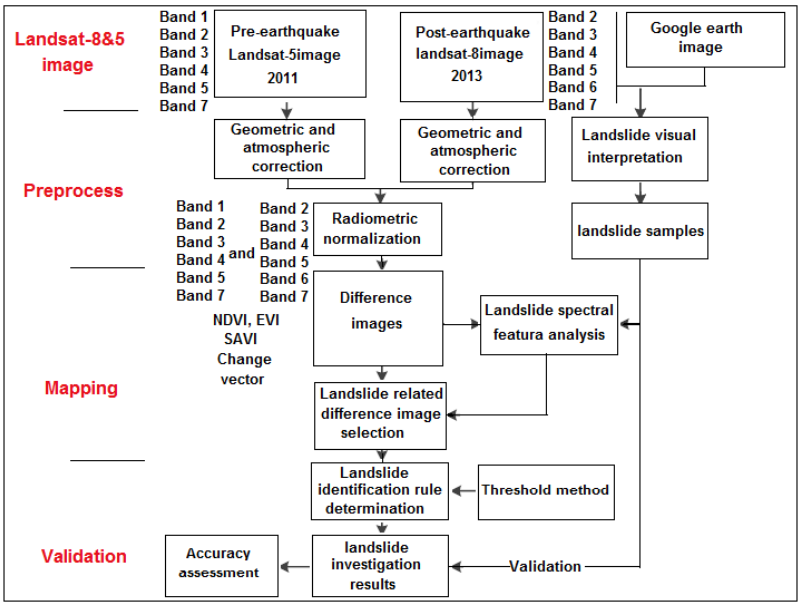

Fig 2. Flowchart of the used semi-automated landslide detection method.

and temporal constraints, radiometric Resolution, atmospheric conditions, vegetation growth, and soil moisture conditions. Therefore, accurate discrimination of the changes from landslides requires the exclusion or reduction of the impacts caused by these other factors. A relative radiometric normalization was conducted using the post-earthquake Landsat-8 image as a reference and the pre-earthquake Landsat-5 image was adjusted to match the radiometric level of the reference image.
Because there are some disturbances from land surface changes, a robust linear regression was performed between the bi-temporal Landsat-8 & 5 images for each study area to obtain the normalization coefficients. The formula is (Zhao et al. 2017) expressed as follows:

$$Obs_{post,\ i} = a_i \cdot Obs_{pre,\ i} + b_i \quad (1)$$

Where Obs*post*, *i* and Obs*pre*, *i* are the surface reflectance for the *i*th band of the post- and pre-earthquake Landsat-8 images, and a_i and b_i are the derived coefficients from the robust linear regression. Areas covered by clouds and shadows are excluded from the linear regression.

2.3.3. Landslide Mapping

Landslide mapping typically uses multitemporal remote sensing data to analyze the temporal effects of phenomena and quantify of the changes. Regarding landslides in these study areas, their major impacts on the surface are the disturbance of vegetation cover and the exposure of soil and rock. The associated damage is more serious in regions with steep slopes in the high mountain areas. Therefore, the investigation was majorly conducted based on the spectral differences between vegetation and bare surfaces.

2.3.4. Image Difference Calculation

Before landslide identification, an important step is to obtain the difference images for bands or spectral indices related to geo-hazards. Considering the disturbance of vegetation cover by landslides, three vegetation indices, including the normalized difference vegetation index (NDVI), the Enhanced vegetation index (EVI), and the Soil adjusted vegetation index (SAVI), were calculated. Then, the difference images were derived for the surface reflectance of band 1to band 7 except band 6 for Landsat-5 and band 2 to band 7 for Landsat-8 and the vegetation indices were calculated to the equations(Zhao et al. 2017) as follows:

$$Diffb(X) = SRb,post(X) - SRb,pre(X) \quad (2)$$

b=(band 2.3.4 .5.6.7 landsat 8) and (band 1.2.3.4.5.7 Landsat5)

$$Diffvi(X) = VIpost(X) - VIpre(X)$$

(VI = NDVI, EVI, or SAVI)

Where SRb, pre (X) and SRb, post (X) are the surface reflectance values of the pre- and post-earthquake images for pixel X, b represents a band number, and VIpre (X) and VIpost (X) are the pre- and post-earthquake vegetation indices for pixel X. In addition to the difference images from each individual band, the change magnitude of the integrated spectral feature differences is calculated based on the change vector. Two vectors Vpre and Vpost can be defined according to the six bands for the pre- and post-earthquake Landsat-5 and Landsat-8 data, and the change vector is determined by the differences between them:

$$CV = V_{post} - V_{pre} = \begin{bmatrix} SR_{1,post} - SR_{1,pre} \\ SR_{1,post} - SR_{1,pre} \\ SR_{2,post} - SR_{2,pre} \\ \dots \\ SR_{6,post} - SR_{6,pre} \end{bmatrix} \quad (3)$$

The magnitude of the change vector (MCV) is then calculated by following expression:

$$MCV = \sqrt{\sum_{b1}^{n} (SR_{b,post}(X) - (SR_{b,pre}(X))^2} \quad (4)$$

b=(band 2 ,3,4 ,5,6,7 landsat 8) and (band 1,2,3,4,5,7 Landsat5)

It is clear that the band differences only reflect the changes in a single band, while the MCV contains information from all the included bands. Ideally, a pixel that has undergone no change will record a value of zero for all values, and their absolute values represent the magnitude of the change between the post- and pre-earthquake images. However, there is still one obvious difference between the band difference and the MCV. Both positive and negative pixel values can be found in the band difference images, and the positive and negative signs represent different directions of changes. The MCV only measures the size of the change without directional information.

2.3.5. Threshold Determination for Change Detection

The difference images obtained using the above-mentioned expressions should include changes caused by earthquake-induced landslides. However, the differences are still affected by errors from imprecise orthorectification, differences in phonological state, atmospheric conditions, illumination and view angles, and soil moisture. Although the radiometric normalization reduces the impacts of these factors, but influences cannot be ignored. So for reducing the uncertainty related to these impacts, a threshold method is employed in this study. This method is reflected by the following expression:

$$\rho(X) = \begin{cases} \text{Landslide, } (\rho(X) \geq V \text{ threshold}) \\ \text{Background, } (\rho(X) < V \text{ threshold}) \end{cases} \quad (5)$$

If the image difference value ρ(X) of pixel X is greater than or equal to the threshold V threshold, the pixel is labeled a landslide candidate; otherwise, the pixel is labeled a background pixel. It is clear that the determination of the threshold value plays a critical role in this method. Usually, the selection of a threshold to identify a changed or unchanged pixel can be done empirically through experience or objectively through an optimal threshold search algorithm. According to the landslide inventory study by Li et al. (2016) the threshold value is expressed as:

$$V\ threshold = \bar{\rho} + \alpha \times \sigma \quad (6)$$

Where $\bar{\rho}$ and σ are the mean and standard deviation of ρ, respectively. α is a free parameter representing a multiplier applied to the standard deviation. According to this formula, the parameter α plays a critical role in determining the final geo-hazard identification accuracy. Usually, a comparative experiment is done to compare the detection performances with different α values, and the final value is chosen based on this experiment.

2.3.6. Validation

To effectively validate the landslide mapping accuracy, both Google Earth images and the original Landsat-8 data were used. High spatial resolution Digital-Globe images acquired after the earthquake were provided by Google Earth (http://www.earth.google.com). Visual interpretation was conducted to identify earthquake-induced landslides in both study areas. Then, visual assessment was applied to check the accuracy by comparing the mapping results, and the landslide samples as introduced in the flowchart. Finally, the validating results obtained by using the error matrix.

3. Results asd discussion

3. 1. Radiometric Normalization

Figure 3 shows the density plots from the band (1,2,3,4,5,7 for Landsat-5 and 2,3,4,5,6,7 for Landsat-8) for the pre-earthquake and post-earthquake images in the study area. Good linear relationships can be observed between the bi-temporal surface reflectance.

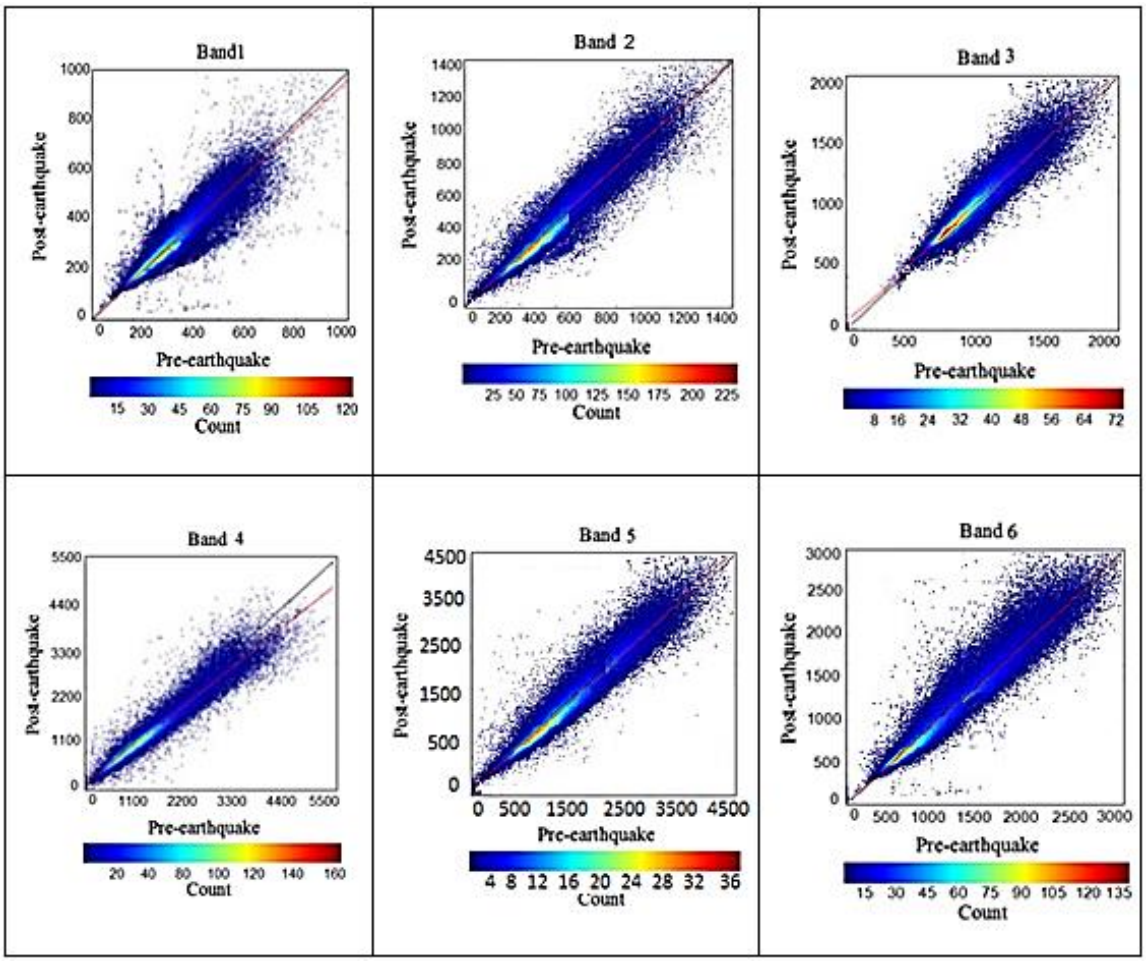

Fig 3. Density plots for band (1,2,3,4,5,7 for Landsat-5 Equal to 2,3,4,5,6,7 for Landsat-8 = band 1 to 6) surface reflectance (∗10000) for the pre- and post-earthquake Landsat 5 and 8 images in study area.

According to the radiometric normalization method introduced in this study, a linear regression method was first applied to the dataset to reduce the influence of outliers. Table. 1. Lists the linear regression results of the six bands in the study area. The R2 values of study area change from 0.6745to 0.9432, with the root mean square deviation (RMSD) ranging from 0.0032 to 0.0186. The equation of RMSD is:

$$\text{RMSD}=\sqrt{\frac{1}{N}}\sum_{i=1}^{N}\delta_i^2 \quad (7)$$

is the distance between pixel *i* and either a reference structure or the mean position of the *N* equivalent pixels. It should be noted that in order to equate bands of Landsat 5 and 8, the similar and equal bands will be called 1 to 6 in throughout of the paper. Of R^2 reflects good correlation between the bi-temporal images. However, among these six bands, there are still some obvious differences, especially for band 4. The points in band 4's density plot for the study area are much more dispersed than those of other bands, with relatively low R2 and the highest RMSD. This result means that there are many factors inducing the high uncertainty during this regression. In the study area, the regression lines are very close to the 1:1 ideal regression line except for that of band 4. From the density plots, it can be learned that although the radiometric differences in the study area for different bands are quite different, it is still necessary to conduct radiometric normalization between the bi-temporal images. According to the regression coefficients, radiometric normalization was performed to recalibrate the pre-earthquake Landsat-5 data to the same level as the post-earthquake Landsat-8 data in the study areas.

Table 1. Liner Regression coefficients of the bi-temporal Landsat-8 & 5 data for Band 1 to 6 in study area.

Band No.	a	b	R^2	RMSD
1	0.9441	0.0015	0.8944	0.0032
2	0.9517	0.0017	0.9145	0.0165
3	0.9835	0.0041	0.9222	0.0050
4	0.8968	-0.0024	0.6745	0.0186
5	0.8785	0.0100	0.9121	0.0056
6	1.001	0.0021	0.9432	0.0064

3.2. Difference Images Calculation

Difference images were calculated with the pre and post-earthquake Landsat-5 and Landsat-8 data, including the band differences of the band reflectance images (1,2,3,4,5,7 for Landsat-5 Equal to 2,3,4,5,6,7 for Landsat-8 = band 1 to 6), the three vegetation index difference images (NDVI, EVI, and SAVI), and the MCV image Were derived from all six bands difference images. Fig. 4 shows the different images in the study area with the natural color Landsat-8 image in 2013 as the background. The colorbars indicate that the value ranges of the images with a width of two standard deviations. Based on prior knowledge about changes related to earthquake-induced landslides, the Red to Red-Orange areas are highly suspect. To visually inspect the differences in detail, two sub regions, A and B, are selected for closer inspection of the change detection results in all the difference images. Sub region A is in the Southwest part of the study area and Sub region b is located in the middle part of the study area and the Satarkhan Dam is located in this sub region. Generally, the colorbars of Fig. 4 clearly indicate the magnitude of the changes varies for different bands, which shows the different sensitivity of each band to surface changes. Big change ranges can be observed for band 4 to band 6, where as band 1 to band 3 have relatively small change ranges. However, for band 1 to band 3, band 5 and band 6, the difference images exhibit almost the same ability to represent land surface changes related to landslides. The zoomed-in images of sub region b shows similar patterns of surface changes, whereas sub region A is contaminated by errors in the original data of band 1 to band 3 with very coarse pixels observed for this region. Comparatively, the changing areas detected by the difference image of band 4 are quite inconsistent with those of other five bands. It is attributed to the high sensitivity of band 4 to vegetation growth, and the detected changing areas are mixed with vegetation cover differences and landslide induced changes.

Regarding the vegetation index difference images, the changing patterns are very similar. However, compared with the spectral differences, the vegetation index difference images also suffer from variations in vegetation phenology, especially for the downstream of the river. When comparing the MCV image with the other difference images, we find that the integration of the differences in all spectral bands ensures that the change vector method captures land surface change well.

3.3. Results of Landslide Mapping

According to the difference detection results for the study area shown in Fig 4, it can be concluded that it is difficult to directly identify areas prone to landslides from a single difference image. The changing areas that are related to landslides are mixed with surface changes induced by other factors, especially vegetation phenology differences. The comparison study indicates that the band difference images (except for band 4) are less disturbed by vegetation growth differences than other difference images. This conclusion is supported by the band differences of landslide pixels shown in Fig. 5. Six sampling pixels in landslide-influenced areas were selected as examples to present the band surface differences between post and pre-earthquake images. It is clear that the band reflectance values (except for band 4) have significant increases due to the exposure of bare soil or rocks by landslide. In contrast, the surface reflectance in band 4 is highly correlated with vegetation cover, and it has an opposite change direction. Negative values can be observed for this band.

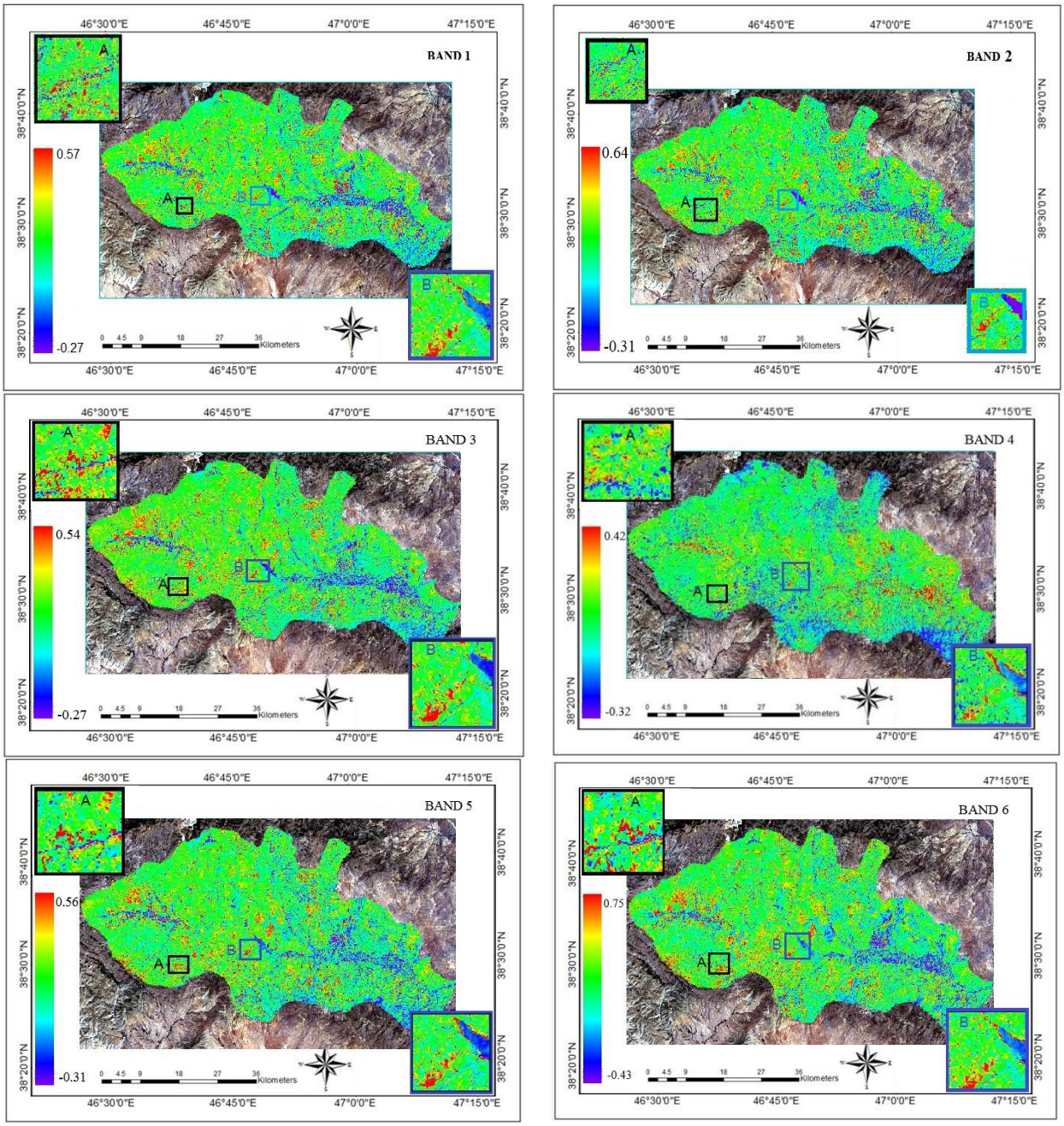

Fig 4. Difference images of study area based on pre- and post-earthquake Landsat-5 & Landsat -8 data.

Therefore, according to the spectral variation characteristics of the six bands that contain information on landslides, a simple model, proposed by (Zhao et al. 2017), was used to measure the bi-temporal reflectance changes. The model is expressed by the following equation:

$$\text{Diff} = \sum_{i=1}^{7}(\rho_{i.post} - \rho_{i.pre})(i \neq 4) / \sum_{i=1}^{7}\rho_{i.post}\,(i \neq 4) \quad (8)$$

Where Diff is the value that measures the changes, $\rho i_{,\,post}$ is the post-earthquake surface reflectance, $\rho i_{,\,pre}$ is the pre-earthquake surface reflectance, and I represent the band number. The model enhances the reflectance differences by calculating the sum of the five band differences, and then normalizes by the sum of the spectral differences of the five bands.

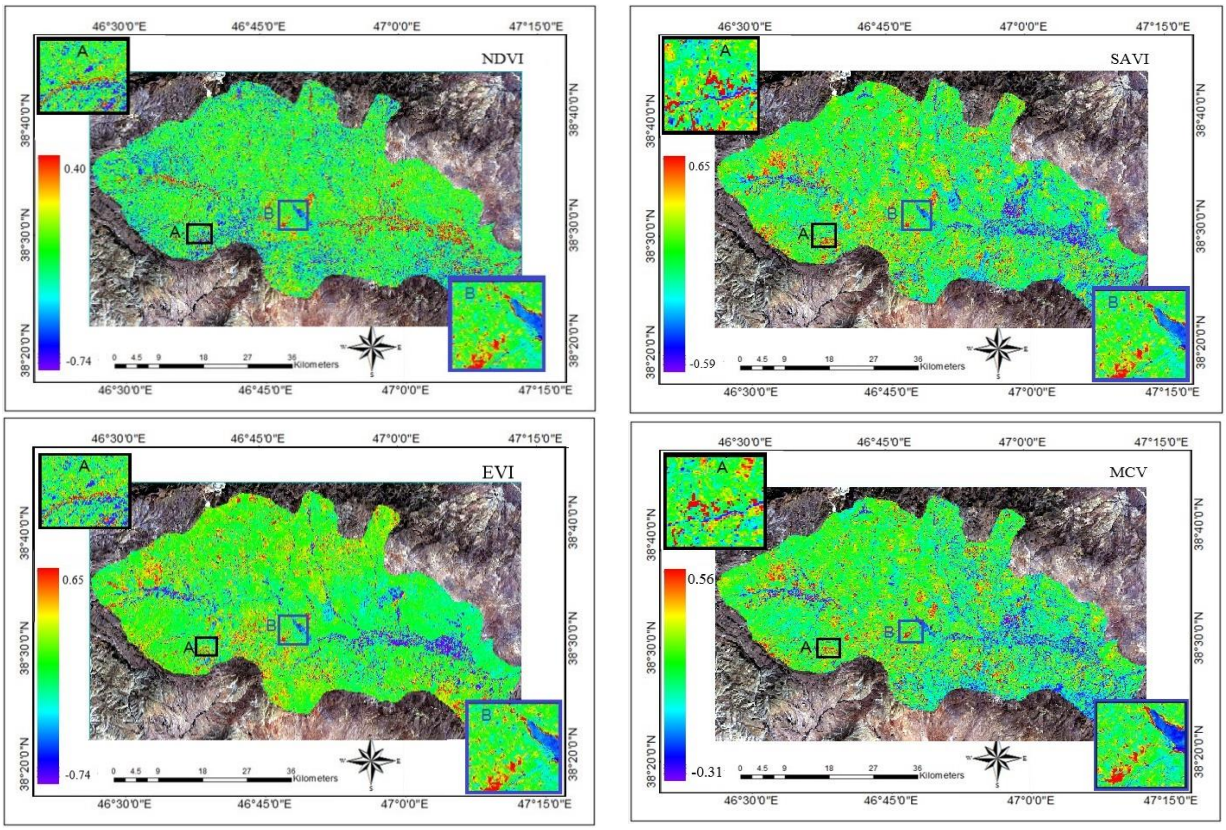

Fig 4. Continued

The spectral information about vegetation in band 4 is not included in the model to reduce the influence of vegetation phenology differences. Meanwhile, the normalization, similar to the relative change calculation, is helpful be helpful for describing the magnitudes of the identified changes. The difference maps for the study area derived by the used model are shown in Fig 6. Compared with the simple band difference images in Fig 4, the difference images in Fig 6 shows better ability to suppress the disturbances from vegetation growth and other factors. The land surface changes induced by the occurrence of landslides can be clearly identified in these difference images. Based on the difference images in Fig 6, the threshold method was applied to identify the changes induced by landslides. As described in the methods section, a comparative experiment with the value of α changing from 1.0 to 4.0 was conducted for the study area. Clearly, errors involving the false identification of geo-hazard related features will decrease with increasing values of α. However, some real geo-hazardous areas will be eliminated at the same time. Therefore, an appropriate value of α should be determined to make a compromise between the investigation accuracy and the missing identification. Based on the comparative experiment, the value of α was set to 1.5 and. 3.5 for the study area, respectively, and the threshold value was chosen to enable accurate mapping of the landslide areas. Fig 7 shows the landslide mapping results in the study area. It shows that the landslide-prone areas are primarily located in the valleys along the river and roads, and greatly threaten the safety of people and goods moving along the road and the local villages along the roads and valleys. Regarding the spatial distribution, the landslides are mainly distributed in the middle to north and south part in the study area. The high mountain topography with deep valleys and steep slopes causes slope instability and earthquake-triggered landslides.

3. 4. Validation

3.4.1. Validation of results using Google Earth Images

To effectively validate the landslide mapping results, we used high-resolution images from Google Earth provided by Digital- Globe that were acquired before the earthquake and the original Landsat-8 images to quantitatively evaluate the investigation accuracy.

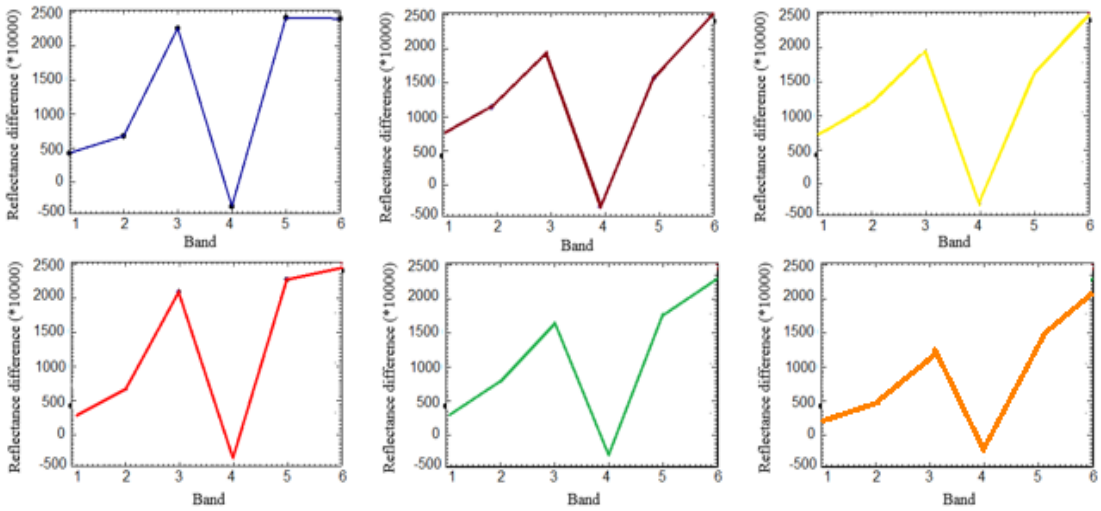

Fig 5. Band differences for six sampling pixels in geo-hazard-affected areas.

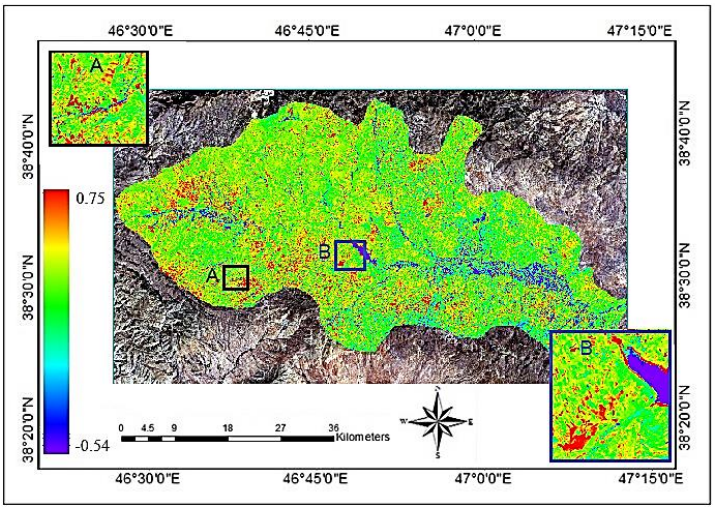

Fig 6. Difference images of study area derived with the used model.

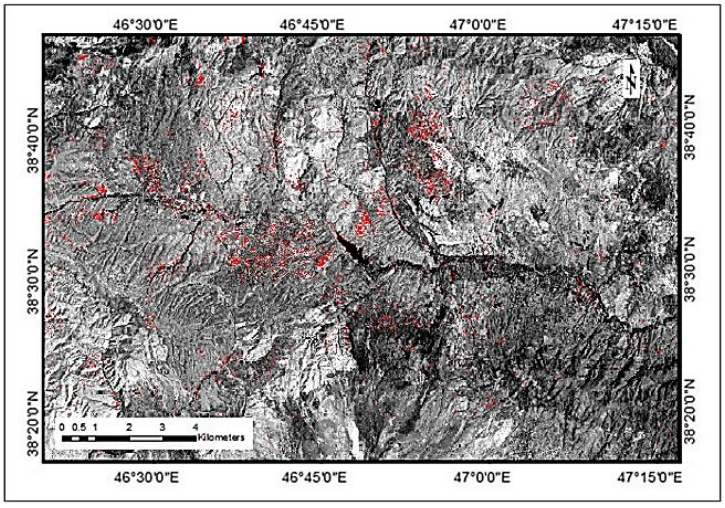

Fig 7. Landslides investigation results (Red color areas) for study area.

Figures 8 and 9 show the visual validation results for the two sub-regions in the study area. The red arrows point out the corresponding relationship between the detected landslides of all sub-regions and the landslides digitized in the Google Earth images. It is obvious that the investigation results are quite consistent with the manual explanation results from high-resolution images. Meanwhile, the comparison of the pre and post-earthquake true color images used in this study also clearly represents changes due to the occurrence of landslides. It is clear that the big linear landslide can be accurately identified by the used method as shown in Figs. 8 and 9. The validation results truly support the good performance of the used method.

3.4.2. Accuracy Assessment of the Results of the Slope instabilities

In summary, 133 control ground points were collected from five classes of unstable slopes In Google earth to validate experiment. The selection of points was based on the accessibility and the homogeneity of the samples. The accuracy of the map was obtained through the confusion matrix using all the 133 points (Table 2). Overall accuracy reached 92.1%, with a kappa coefficient of 0.99. The accuracy of non-instability reached 100%, whereas the class of extreme instability reached 89.25%. Results indicate that the implication vegetation coverage fractions in a feature space can be a feasible and useful tool for assessment and identifying of changed areas (Table 3). The errors of omission represent pixels that belong to the ground truth class. However, the classification technique failed to classify them into the proper class. The errors of commission represent pixels that belong to another class, which are labelled as belonging to the class of interest.

3.5. Spatial Distribution Analysis

Quantitatively analyzing the spatial distribution of the landslides induced by this big earthquake was conducted based on the Aster 30 m DEM data. Fig 10 presents the histogram maps of the elevation and slope information related to detected landslides in the study area. The large landslide in south of the study area is excluded from this analysis because it occurred before the earthquake. It can be realized that most of the landslides occurred in areas of steep slopes. The landslides in the study area are mostly distributed in areas with slopes ranging from 15° to 40°, with an average value of 36.02°. In addition to the topographic analysis against the investigation results, the changes in NDVI of the landslide areas also clearly present the influence of the landslides on surface vegetation cover. As discussed in the previous section, the major impacts of the occurrence of landslide are the destruction of surface vegetation cover and the exposure of bare surfaces. The pre- and postearthquake histogram of the NDVI values in the landslide areas shown in Fig. 10 clearly indicates these changes with significant decreases in NDVI distribution. The mean NDVI values of these slope instabilities areas change from 0.5893 to 0.3400 for study area.

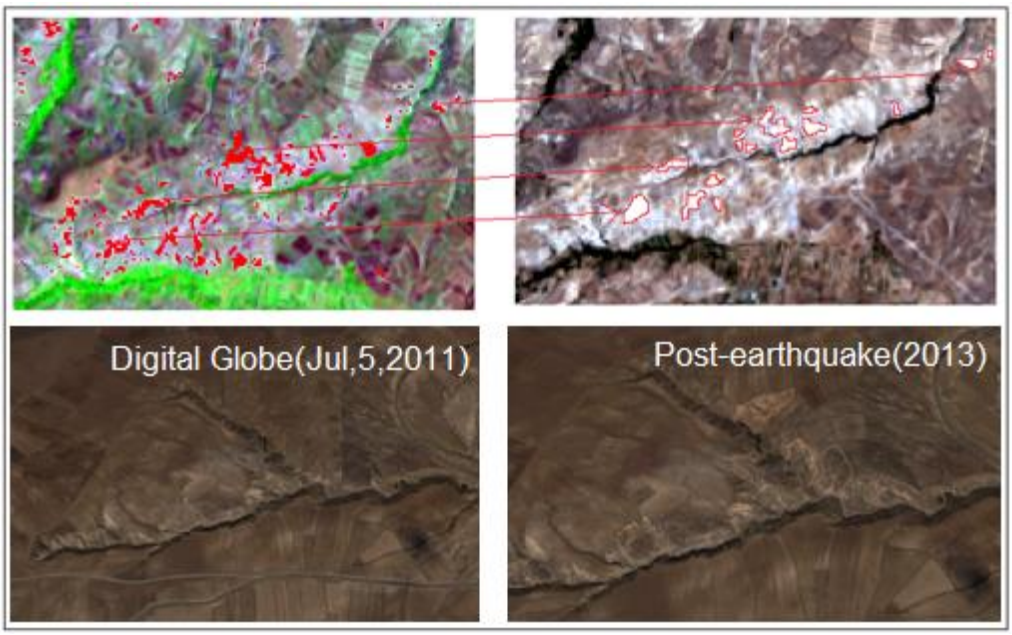

Fig 8. Visual validation of the landslide investigation results in the sub-region A of study area with high-resolution Digital-Globe images from Google Earth and pre- and post-earthquake Landsat-8 and Landsat-5 images.

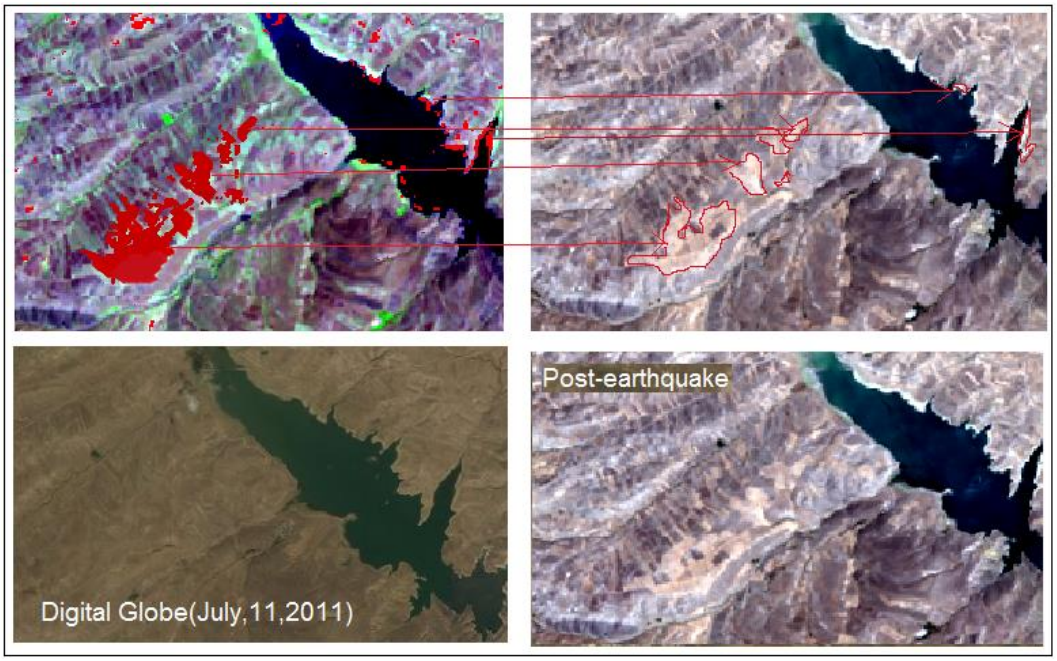

Fig 9. Visual validation of the landslide investigation results in the sub region B of study area with high-resolution Digital Globe images from Google Earth and pre- and post- earthquake Landsat-8 and Landsat-5 images.

Table 2. The confusion matrix

Classes	Non	Low	Moderate	Severe	Extreme	Total
Non	25	0	0	0	0	25
Low	0	33	0	0	0	33
Moderate	0	2	20	1	0	23
Severe	0	0	1	20	3	24
Extreme	0	0	0	3	25	28
Total	25	35	21	24	28	133

Ground Truth **(%)**

Classes	Non	Low	Moderate	Severe	Extreme	Total
Non	100	0	0	0	0	18.8
Low	0	94.28	0	0	0	24.81
Moderate	0	5.71	95.23	4.17	0	17.30
Severe	0	0	4.77	83.33	10.71	18.04
Extreme	0	0	0	12.5	89.29	21.05
Total	100	100	100	100	100	100

Regarding the elevation, most of the landslides in the study area fall within the range of 1420–2000 m, with an average value of 1843 m. regarding of the histograms indicates that the landslides in the study area are generally distributed over higher elevation areas with steeper slopes. Figure 11 shows some of the slope instabilities due to from the earthquake 2012 on the slopes located on the north of the Dopeyag village.

Although the validation partly confirms the ability of the used method, ability for identifying the locations and magnitude of landslides with relatively high accuracy, there are still some constraining factors that influence the method accuracy.

It is verified that the used method is able to detect landslides over relatively large areas. However, a closer examination of the results shows many pixel-level geo-hazards, and it is hard to check their real situation. For these small-scale geo-hazards, the relatively large size of Landsat-5 and Landsat-8 pixels (30 m) may include mixed information from the landslides and the adjacent, unchanged natural surfaces, resulting in smaller surface reflectance changes than those associated with middle to large scale geo-hazards. Therefore, it is hard to fully discriminate the landslides at small scale from other surfaces. So, the pixel resolution becomes an important limitation for small-scale geo-hazard investigation. It also indicates that the spatial resolution of the remote sensing data used in landslide investigations strongly influences the survey accuracy.

In present study two Landsat-5 & Landsat-8 remote sensing data were used (June 5 and August 11) acquired in the same season or nearly the same season in 2011 and 2013, respectively, to represent the pre and post-earthquake images to reduce the impacts of seasonal and phonological variation. There is about a one-year gap between two images.

Table 3. Classification accuracy of the map of desertification degrees.

	Commission (percent)	Omission (percent)	Commission (pixels)	Omission (pixels)
Non	0	0	0/25	0/25
Low	0	5.71	0/33	2/35
Moderate	13.04	4.76	3/23	1/21
Severe	16.66	16.66	4/24	4/24
Extreme	10.71	10.71	3/28	3/28
	Pro Acc (percent)	User Acc (percent)	Pro Acc (Pixels)	User Acc (Pixels)
Non	100	100	25/25	25/25
Low	94.28	100	33/35	33/33
Moderate	95.24	86.95	20/21	20/24
Severe	83.33	83.33	20/24	20/24
Extreme	89.25	89.25	25/28	25/28

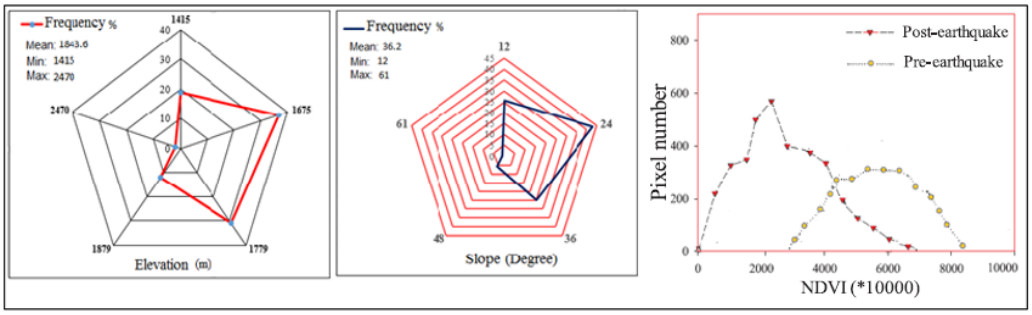

Fig 10. Histograms of the slope and elevation and NDVI of the identified landslides in study area.

Fig 11. Slope instabilities due to the earthquake 2012 (Slopes located on the north of Dopeyag village).

Therefore, the final change detection results contain surface changes not only caused by earthquake-induced landslides, but also induced by other natural hazards and human activities (deforestation and villageation). These later changes should be regarded as errors when only considering the earthquake-induced landslides investigation; however, it is difficult to discriminate them from the investigation results. For example, there is a landslide recognized by the used method in the study area. In reality, these landslides occurred in between the two remote sensing data acquisition dates and they were induced by rainfall not the earthquake. Consequently, although the used method is able to identify landslides, the big time gap between the bi-temporal remote sensing data will introduce uncertainty in the final investigation results, and the individual landslides should be checked whether they are induced by the earthquake with remote sensing data acquired during this period. The study area is located in a typical mountain environment; the mentioned area is limited to the Arasbaran forests to the north, the eastern slopes of the Owrtat Sakhvor Mountain to the east, the eastern slopes of the Kohnaloo Mountain to the west and the Aji Chai basin to the south. It is well known that slopes facing toward the sun usually receive more light and appear brighter than slopes facing away from the sun. The illumination of remote sensing data is greatly modified by topography, and the proportion of light reflected toward the satellite varies with the geometry of the sun, target, and viewer (Shepherd and Dymond 2003, Szantoi and Simonetti 2013, Zhao et al. 2017). The topographic effect on remote sensing data greatly influences their use in the quantitative analysis. Therefore, the topographic effect on Landsat- 5 and Landsat -8 data used in this study introduces large uncertainties into the final investigation results. This influence is even more serious in areas covered by shadow, which can be observed from the sub- region images shown in Figs. 8 and 9. The weak signal in the shadow region not only partly distorts the real surface reflectance spectra, but also prevents accurate detection of changes in the shadow region. Therefore, an effective topographic correction should be applied to remote sensing data before its usage for geo-hazard investigations in mountainous areas.

4. Conclusion

This study used the pixel-based change detection method for mapping landslides induced by the 2012 ahar-varzegan earthquake in the study area from ahar to varzegan by using the multispectral information from pre- and post-earthquake Landsat-5 and Landsat-8 remote sensing data. The validation results indicated that the used method was able to identify the landslides with a relatively high accuracy and Landsat-5 and Landsat-8 images can be used as a good data source for landslides investigation because of its multispectral advantage. The accuracy of the map was obtained through the confusion matrix using all the 133 points Overall accuracy reached 92.1%, with a Kappa coefficient of 0.99. The mapping results suggested that the landslides were mostly located along the river valleys and roads in the high mountain areas with deep valley and steep slopes. Although the study shows that this method has potential for investigating earthquake-induced landslides, there are still some problems that should be noted: 1) the relatively coarse spatial resolution of Landsat-5 and Landsat-8 data limits the method's ability to recognize small-scale landslides, 2) although the use of images separated by almost exactly one year reduces confounding effects from vegetation phenology differences, the change detection results reflect all the landslide events during this year. Landslides that occurred before the earthquake will be included in the detection results. Therefore, the incorporation of high spatial resolution remote sensing data are helpful for identifying small-scale landslides, and the determination of the individual landslides occurring is very important for real-time disaster assessment and relief.

Acknowledgement

The authors would like to acknowledge the University of Tabriz and the Iran national Science foundation, Science deputy of presidency, for their support and contribution to this research
and the present paper..

References

Callaghan K, Engelbrecht J, Kemp J (2015) the Use of Landsat and Aerial Photography for the Assessment of Coastal Erosion and Erosion Susceptibility in False Bay, South Africa. *South African Journal of Geomatics* 4: 65-79.

Ciampalini A, Federico R, Bianchini S, Frodella W, Bardi F (2015) Remote Sensing As A Tool For Development Of Landslide Databases: The Case Of The Messina Province (Italy) Geodatabase. *Geomorphology* 249:103-118.

Djamour Y, vernant P, Nankali H R, Tavakoli F (2011) NW Iran-Eastern Turkey Present-Day Kinematics: Results From The Iranian Permanent GPS Network. *Earth and Planetary Science Letters* 307**:** 27-34.

Dou J, Chen S, Chang K T, Yunus A P (2015) Automatic Case-Based Reasoning Approach For Landslide Detection: Integration Of Object- Oriented Image Analysis And A Genetic Algorithm. *Remote Sensing* 7: 4318- 4342.

Huang Y, Chen W, Liu J (2012) Secondary Geological Hazard Analysis in Beichuan after the Wenchuan Earthquake and Recommendations for Reconstruction. *Environmental Earth Sciences* 66: 1001-1009.

Jaboyedoff M, Oppikofer T, Abellán A, Derron MH, Loye A, Metzger R, Pedrazzini A (2012) Use of LIDAR in Landslide Investigations: A Review. *Natural Hazards* 61: 5-28.

Keefer DK (1984) Landslides caused by earthquakes, *GeologicalSociety of America Bulletin*, 95: 406-421.

Lacroix P (2016) Landslides Triggered by The Gorkha Earthquake In The Langtang Valley, Volumes And Initiation Processes Earth, *Planets Space* 68: 1- 46.

Lacroix P, Zavala B, Berthier E, Audin L (2013) Supervised Method of Landslide Inventory Using Panchromatic SPOT5 Images And Application to The Earthquake-Triggered Landslides Of Pisco (Peru, 2007, Mw8. 0). *Remote Sensing* 5: 2590-2616.

Li Z, Shi W, Myint S W, Lu P, Wang Q (2016) Semi-Automated Landslide Inventory Mapping From Bi-temporal Aerial Photographs Using Change Detection And Level Set Method. *Remote Sens Environ* 175: 215 - 230.

Martha TR, Govindharaj KB, Kumar K V(2015) Damage and Geological Assessment Of The 18 September 2011 M W 6.9 Earthquake In Sikkim, India Using Very High Resolution Satellite Data. *Geosciences* 6: 793-805.

Milillo P, Fielding EJ, Shulz WH, Delbridge B, Burgmann R (2014) COSMO-Skymed Spotlight Interferometry Over Rural Areas: The Slumgullion Landslide In Colorado, USA. *IEEE Journal of Selected Topics in Applied Earth Observations and Remote Sensing* 7: 2919-2926.

Moosavi SH, Ranjbar A (2014) Monitoring and Tracking of Land Use Changes in Cloud Mountain Basin Using Satellite Images. *Journal of Geographical Information*: 25(97) : 130- 145 .

Moosavi V, Talebi A, Shirmohammadi B (2014) Producing a Landslide Inventory Map Using Pixel-Based And Object-Oriented Approaches Optimized By Taguchi Method. *Geomorphology* 204: 646-656.

Nichol J, Wong M S (2005) Satellite Remote Sensing For Detailed Landslide Inventories Using Change Detection And Image Fusion. Int. J. *Remote Sensing* 26: 1913-1926.

Petschko H, Bell R, Glade T (2015) Effectiveness Of Visually Analyzing Lidar DTM Derivatives For Earth And Debris Slide Inventory Mapping For Statistical Susceptibility Modeling. *Landslides* 13: 1-16.

Rastner P, Bolch T, Notarnicola C, Paul F (2014) A Comparison of Pixel and Object-Based Glacier Classification with Optical Satellite Images. *IEEE Journal of Selected Topics in Applied Earth Observations and Remote Sensing* 3: 853-862.

Roostaei Sh (2000) A Study On The Dynamics Of Landslides and The Causes Of Their Occurrence Using Morphometric Methods In Aharchay Basin. Ph.D. Thesis, Rajaei, Abdolhamid. *Tabriz University.*

Seed HB (1968) Landslides during earthquakes due to soil liquefaction, *Jurnal of the soil mechanice and foundations division, American society of civil engineers* 93(SM5): 1053-1122.

Shepherd J, Dymond J (2003) Correcting satellite imagery for the variance of reflectance and illumination with topography. *Remote Sensing* 24: 3503–3514.

Shi B, Liu C (2015) Uav for Landslide Mapping and Deformation Analysis. Proc. I*nternational Conference on Intelligent Earth Observing and Applications* 9808:12.

Szantoi Z, Simonetti D (2013) Fast and robust topographic correction method for medium resolution satellite imagery using a stratified approach." *IEEE Journal of Selected Topics in Applied Earth Observations and Remote Sensing* 6(4): 1921–1933.

Travelletti J, Allemand P, Delacourt Ch, Malet JP (2012) Correlation Of Multi-Temporal Ground-Based Optical Images For Landslide Monitoring: Application, Potential And Limitations. ISPRS J. Photogramm. *Remote Sensing* 70: 39-55.

Vermote E, Justice C, Claverie M,Franch B (2016) Preliminary analysis of the performance of the landsat 8/OLI and surface reflectance product. *Remote Sensing Enviroment* 185: 46-56.

Wei Y, Wei X, Chen Y (2014) Analysis of Distribution Regularity and Development Tendency of Earthquake Secondary Geo-Hazards in Yingxiu - Maoxian Section along the Minjiang River. *Remote Sensing*. Land Retour 26: 179-186.

Xu C (2015) Preparation of Earthquake-Triggered Landslide Inventory Maps Using Remote Sensing And GIS Technologies: Principles And Case Studies, *Geoscience Frontiers* 6: 825-836.

Yazdi P, Escribanoa J, Santoyo M (2017) Stress transfere and statistical analysis of 2012 aharvarzeghan. Seismic sequnce, northwestern Iran. *Primer Congreso en Ingeniería Geomática. Valencia,* 5 - 6 de Julio 2017.

Zhan Z, Lai B (2015) a Novel DSM Filtering Algorithm for Landslide Monitoring Based On Multiconstraints. *IEEE Journal of Selected Topics in Applied Earth Observations and Remote Sensing* 8: 324-331.

Zhao W, Li A, Nan X, Zhang Z, Lei G (2017) Postearthquake landslides Mapping from landsat-8 data for the 2015 Nepal earthquake. *IEEE Journal of Selected Topics in Applied Earth Observations and Remote Sensing* 10(5): *1758-1768.*